

Accepted to AJ

Local Group Dwarf Elliptical Galaxies: I. Mapping the Dynamics of NGC 205 Beyond the Tidal Radius

M. Geha¹

*The Observatories of the Carnegie Institute of Washington, 813 Santa Barbara Street, Pasadena,
CA 91101.*

mgeha@ociw.edu

P. Guhathakurta

*UCO/Lick Observatory, University of California, Santa Cruz, 1156 High Street, Santa Cruz,
CA 95064.*

raja@ucolick.org

R. M. Rich

Department of Physics and Astronomy, UCLA, Box 951547, Los Angeles, CA 90095.

rnr@astro.ucla.edu

M. C. Cooper

*Department of Astronomy, University of California at Berkeley, 601 Campbell Hall, Berkeley, CA
94720-3411.*

cooper@astron.berkeley.edu

ABSTRACT

NGC 205 is the nearest example of a dwarf elliptical (dE) galaxy and the prototype of this enigmatic galaxy class. Photometric evidence suggests that NGC 205, a close satellite of the M31 galaxy, is tidally interacting with its parent galaxy. We present stellar radial velocity measurements out to a projected radius of 20' (5 kpc) in NGC 205 based on Keck/DEIMOS multislit spectroscopic observations of 725 individual red giant branch stars. Our kinematic measurements extend from the center out to six times the effective radius of NGC 205, well past the expected tidal radius. The contamination

¹Hubble Fellow.

in our kinematic sample from M31 field stars is estimated to be a few percent based on maximum likelihood fits to the distribution of stars in position-velocity space. We measure a maximum major-axis rotation speed for the body of NGC 205 of 11 ± 5 km s $^{-1}$ and note that this is based on observing a definite turnover in the rotation curve; this is the first dE galaxy in which the maximum rotation velocity has been measured. Combined with the velocity dispersion, we conclude that NGC 205 is supported by a combination of rotation and anisotropic velocity dispersion. At a major-axis distance of $4.5'$ (1 kpc), the velocity profile of NGC 205 turns over; stars beyond this radius are moving counter to the rotation of the inner part of the galaxy. The turnover radius is coincident with the onset of isophotal twisting and the estimated tidal radius, suggesting that the outer kinematics of NGC 205 are dominated by gravitational interactions with the nearby M31 galaxy. The motion of stars beyond a radius of $\sim 4.5'$ implies that NGC 205 is in a prograde encounter with its parent galaxy M31.

Subject headings: galaxies: dwarf — galaxies: kinematics and dynamics — galaxies: individual (NGC 205) — galaxies: interactions

1. Introduction

NGC 205 is a low-luminosity, early-type, dwarf galaxy in the Local Group and is one of the brightest nearby examples of a dwarf elliptical (dE) galaxy. A close satellite of the large spiral galaxy Andromeda (M31), NGC 205 has a projected separation to M31 of merely $40'$ or 8 kpc (Fig. 1); the physical separation between NGC 205 and M31 is estimated to be ~ 40 kpc (Demers et al. 2003; McConnachie et al. 2005). This separation distance is intermediate between that of the Milky Way and its dwarf satellite galaxies Sagittarius (24 kpc; Ibata et al. 1995) and the Large Magellanic Cloud (50 kpc; Freedman et al. 2001). Observational evidence such as isophotal twisting at large radii (Hodge 1973; Kent 1987; Choi, Guhathakurta, & Johnston 2002), recent star formation (Peletier 1993; Cappellari et al. 1999), and a steadily increasing velocity dispersion with radius (Bender, Paquet, & Nieto 1991; Simien & Prugniel 2002) suggests that NGC 205 is tidally interacting with its parent galaxy. However, inside the effective radius, $r_{\text{eff}} = 2.5'$ (0.6 kpc), NGC 205 exhibits regular surface brightness and kinematic profiles typical of a normal dE galaxy. NGC 205 therefore offers a unique opportunity to study both the internal dynamics of a nearby dE galaxy while providing a detailed view of a satellite undergoing disruption.

A crucial question for current galaxy formation theories is to what extent the accretion of dwarf satellite galaxies contributes to the growth of massive galactic halos (Bullock et al. 2000; Font et al. 2005). The M31 galaxy and its associated dwarf satellite system are an excellent laboratory to study this question in detail: M31 is the nearest massive galaxy external to the Milky Way in which current observing techniques are able to resolve individual stars. Ibata et al. (2001) and Ferguson et al. (2002) first detected evidence for tidal streams in the halo of M31 based on wide-

area star-count maps. Guhathakurta et al. (2004) and Ibata et al. (2004) provided confirmation that the stars in these streams are dynamically related and have a small enough velocity dispersion to have feasibly been stripped from a dwarf-sized galaxy. Meylan et al. (2001) have suggested that the globular cluster G1, one of the brightest globular clusters belonging to M31, is the remnant core of a nucleated dwarf galaxy based on its internal dynamics and stellar populations (however see Reitzel et al. (2004)). From these observations, it is clear that dwarf satellite disruption must contribute to the build-up of M31’s halo; detailed study of current, on-going interactions between M31 and its satellites should help quantify what fraction of halo material is attributed to this process.

Galaxy formation scenarios for the origin of dE galaxies lie broadly in two very distinct categories: (1) dEs are old, primordial objects, and (2) dEs have recently evolved or transformed from a progenitor galaxy population (Dekel & Silk 1986; Moore et al. 1998; Mayer et al. 2001; Mastropietro et al. 2004). Dwarf elliptical galaxies are highly clustered (Binggeli et al. 1988)– the majority of dEs in the local Universe are found in dense galaxy clusters. Kinematic studies of dEs in the Virgo and Fornax Clusters suggest a large range in their kinematic properties, from rotationally-supported galaxies to dEs with no detectable major axis rotation (Geha et al. 2003; De Rijcke et al. 2001; van Zee et al. 2004). These results, in particular the abundance of dE galaxies with a complete lack of rotation, have so far been difficult to explain in the context of current formation models. The three bright Local Group dE satellites NGC 205, NGC 147, and NGC 185 provide an excellent opportunity to study dE kinematics in greater detail and to larger radii than their cluster counterparts. In this paper, we present kinematics for the brightest of the Local Group dEs, NGC 205.

The absolute magnitude of NGC 205 is $M_V = -16.5$. It has a nearly exponential surface brightness profile (Choi et al. 2002), characteristic of dE galaxies. As a result, NGC 205 has a far more diffuse appearance than the other bright M31 satellite galaxy, M32, which has a similar absolute magnitude but is classified as a compact elliptical. Near the center of this galaxy, inside a radius of $1'$ (0.24 kpc), NGC 205 contains dust (Haas 1998), atomic and molecular gas (Welch et al. 1998; Young & Lo 1997), and a number of OB associations implying a recent episode of star formation in the past 100 Myr (Peletier 1993; Lee 1996). Beyond this radius, NGC 205 is gas and dust-free and is composed of an intermediate stellar population (Demers et al. 2003), typical for similarly-sized dEs in the Virgo cluster (Geha et al. 2003).

Early dynamical studies suggested that NGC 205 had negligible internal rotation velocity. Dynamical measurements by Bender et al. (1991) placed an upper limit on the rotation velocity of $1.5 \pm 0.8 \text{ km s}^{-1}$ at $\sim r_{\text{eff}}$. Combined with observations of two other Local Group dEs, this established the paradigm that dE galaxies are supported primarily by anisotropic velocity dispersions. However, Simien & Prugniel (2002) more recently measured the major-axis rotation of NGC 205 out to twice the effective radius, measuring a rotation speed $13 \pm 2 \text{ km s}^{-1}$. The central velocity dispersion of NGC 205 has a value of $16 \pm 4 \text{ km s}^{-1}$ (Peterson & Caldwell 1993; Carter & Sadler 1990), increasing with radius to 42 km s^{-1} at $2'$ (Bender et al. 1991) and 50 km s^{-1} at $5'$ (Simien & Prugniel 2002). Assuming an isotropic spheroid model, Bender et al. (1991) inferred a mass-to-light

ratio of $M/L \sim 7$ for NGC 205, similar to the mass-to-light ratios inferred for a sample of Virgo and Fornax Cluster dE galaxies based on more sophisticated dynamical modeling (Geha et al. 2002; De Rijcke et al. 2001). These ratios are consistent with that of a modestly old stellar population with no dark matter. This lack of dark matter in the inner region is in stark contrast to the much larger mass-to-light ratios inferred for fainter dwarf spheroidal (dSph) galaxies in the Local Group, such as the Draco and Ursa Minor dSph, which appear to be dark-matter-dominated even in their central region (Kleyna et al. 2003).

Integrated-light spectroscopy cannot probe the kinematics of dE galaxies much beyond the effective radius due to their characteristic low surface brightness ($\mu_{V,\text{eff}} = 23 \text{ mag arcsec}^{-2}$). Unlike dwarf irregular galaxies, dEs are devoid of gas at large radii so their outer kinematics cannot be studied via HI gas dynamics. Other kinematical probes exist at large radius, such as globular clusters (Beasley et al. 2005) and planetary nebulae (Corradi et al. 2005), but their small numbers make these poor kinematic tracers. The proximity of NGC 205 presents a unique opportunity to study the dynamics of a dE galaxy out to much larger radii than possible in more distant systems: via spectroscopy of individual red giant branch (RGB) stars.

In this paper, we present accurate radial velocities for 725 RGB stars in the Local Group dE galaxy NGC 205 measured via Keck/DEIMOS multi-slit spectroscopy. We present dynamics of this galaxy well beyond the inferred tidal radius, twice the radial extent of previous measurements. This paper is organized as follows: in § 2 we discuss target selection for our DEIMOS slitmasks, the observing procedure and data reduction. In § 3, a detailed kinematic analysis of NGC 205 is presented along with a maximum-likelihood estimate of the kinematic contamination from stars in M31. Finally, in § 4, we discuss the implications of our kinematic observations for the tidal interaction between NGC 205 and M31.

Throughout this paper we adopt a distance modulus to NGC 205 of $(m - M)_0 = 24.58 \pm 0.07$, i.e., a distance of $824 \pm 27 \text{ kpc}$, as determined by McConnachie et al. (2005) via the tip of the RGB method; this places NGC 205 40 kpc further than its parent galaxy M31.

2. Data

2.1. Target Selection

Stars were selected for spectroscopy according to their probability of being a RGB star in NGC 205. Stars were selected based on Canada-France-Hawaii Telescope CFH12K mosaic imaging in the R and I bands kindly provided by Demers, Battinelli, & Letarte (2003, private communication). The CCD mosaic covers a $42' \times 28'$ region centered on NGC 205 with $0.206''$ pixels. The images were obtained in sub-arcsecond seeing conditions. Stellar photometry from these images extends 2 mag below the tip of the RGB. The color-magnitude diagram for this region is shown in Figure 2. A broad RGB is seen extending to very red colors ($R - I > 3.0$); the reddest of these

stars are likely to be metal-rich/reddened M31 disk RGB contaminants (Demers et al. 2003). The vertical ridge near $(R - I) = 0.2$ is due to foreground Milky Way stars. The spatial distribution of stars is shown in Figure 3. The gaps between CFH12K CCD chips are $\sim 7''$ wide. The apparent hole in stellar density map near the center of NGC 205 is due to crowding; the stellar density increase in the lower left corner is due to the presence of field RGB stars belonging to M31.

The absolute magnitude of the RGB is $M_I \sim -4$. At the assumed distance of NGC 205, the apparent magnitude of this stellar population is $I \sim 21$. Since metallicity variations within NGC 205 will cause a spread in the colors of its RGB stars, we select spectroscopic targets based primarily on apparent magnitude. Highest priority in the spectroscopic target list was assigned to stars between $20.5 \leq I \leq 21.0$. Second priority was given to stars between $20.0 \leq I < 20.5$ and $21.0 < I \leq 21.5$; lowest priority was assigned to objects $I > 21.5$. To minimize Galactic foreground contamination, targets were required to have $(R - I) > 0.2$. Stars with photometric errors larger than $\sigma_I > 0.1$ were rejected, as were stars having neighbors of equal or greater brightness within a radius $r < 4''$. The photometric criteria used for spectroscopic target selection are shown in Figure 2.

2.2. DEIMOS Multi-Slit Mask Design

Four multislit masks were observed on the nights of 2003 September 30 and October 1 with the Keck II 10-m telescope and the DEIMOS multi-object spectrograph (Faber et al. 2003). Three of the four masks (N205-1, N205-2, N205-3) were designed to be observed in a conventional mode, while a fourth mask was designed to have multiple tiers of spectra as described in § 2.2.2. Science exposures for all four masks were 3×1200 s per mask; the average seeing FWHM during the spectroscopic observations was $0.7''$.

In Figure 1, the placement of the four DEIMOS slit-masks is shown relative to a Digitized Palomar Optical Sky Survey image of NGC 205. Each DEIMOS multislit mask covers a rectangular area of $\approx 16' \times 4'$. Two slit-masks (N205-1 and N205-4) were positioned on the center on NGC 205 with the long axis of the mask along the major axis of the galaxy. The centers of masks N205-2 and N205-3 were placed $10'$ to the South-East and North-West of NGC 205, respectively. The long axis of these two masks were roughly placed along the direction of tidal distortion. The direction of tidal distortion was determined from surface brightness ellipse fitting by Choi et al. (2002) based on wide-field B -band photometry. The locus of semi-major axes of the ellipse fitting forms a gentle 'S' curve which we plot in Figure 1 and refer to as the major-axis of NGC 205 (see § 3). Slitlets in each mask have the same the position angle as the overall mask—i.e. we did not use tilted slits. In Table 2, we list the observing details for each mask.

2.2.1. Conventional Masks

The three conventional DEIMOS slit-masks (N205-1, N205-2, N205-3) were designed to be observed with the 1200 line mm^{-1} grating covering a wavelength region $6400 - 9100\text{\AA}$. The spectral dispersion of this setup is 0.33\AA , and the resulting spectral resolution, taking into account the anamorphic distortion factor of 0.706, is 1.37\AA (FWHM). This wavelength range includes the Ca II triplet lines which are expected to be strong in absorption for our targeted RGB stars. Slitlets were $0.7''$ wide to match the typical seeing conditions while maintaining good wavelength resolution. The spatial scale is $0.12''$ per pixel and the spectral dispersion of 0.33\AA per pixel. To allow adequate sky subtraction, the minimum slit length was $5''$; the minimum spatial separation between slit ends was $0.4''$ (three pixels).

Using the above input parameters and the target list described in § 2.1, slitmasks were created using the DEIMOS `dsimulator`* slitmask design software. For each slitmask the software starts with the highest priority input targets and automatically fills in the mask area to the extent possible and filling in the remaining space on the slitmask with lower priority targets. An average of nearly 200 slitlets were placed on each mask (see Table 2). A handful of targets were deliberately included on multiple masks. These overlapping targets are used to quantify measurement errors in § 2.4.

2.2.2. Multi-Tier Masks

The DEIMOS slitmask N205-4 was designed for use with a blocking filter centered on the Ca II triplet region. The blocking filter allows multiple tiers of slitlets to be placed on a single mask increasing the observing efficiency by a factor of 2–3 over conventional DEIMOS masks. The Ca II blocking filter has a central wavelength of 8550\AA and is 350\AA wide. In combination with the 831 line mm^{-1} grating, the spectral dispersion of this setup is 0.47\AA , and the resulting spectral resolution is 1.96\AA (FWHM). Two and a half tiers of spectra are possible without significant overlap in the wavelength region $8450 - 8850\text{\AA}$. Three full tiers of spectra are not possible because the DEIMOS field-of-view is narrower in the middle as compared to the ends. The width and typical length of the slitlets are the same as the conventional masks above. This mask was designed by running `dsimulator` three times over the mask. In each pass, slitlets were placed on targets in a row running along the spatial axis of the mask to maximize the number of slitlets. For each pass of `dsimulator`, the region of the CCD detector plane occupied by the spectra of all the slitlets was calculated, the spectroscopic targets in this region excluded, and the resulting target list fed into the next pass. A total of 332 slitlets were placed on the N205-4 mask. The tier pattern of slitlets can be seen in the spatial distribution of targets in Figure 3.

* Available at http://www.ucolick.org/~phillips/deimos_ref/masks.html

2.3. Data Reduction

Spectra from the three conventional DEIMOS multi-slit masks were reduced using the `spec2d` software pipeline (version 1.1.4) developed by the DEEP2 team at the University of California-Berkeley for that survey. A detailed description of the reductions can be found in Cooper et al. (2006). Briefly, the flat-field exposures are used to rectify the curved raw spectra into rectangular arrays by applying small shifts and interpolating in the spatial direction. A one-dimensional slit function correction and two-dimensional flat-field and fringing correction are applied to each slitlet. Using the DEIMOS optical model as a starting point, a two-dimensional wavelength solution is determined from the arc lamp exposures with residuals of order 0.01\AA . Each slitlet is then sky-subtracted exposure by exposure using a B-spline model for the sky. The individual exposures of the slitlet are averaged with cosmic-ray rejection and inverse-variance weighting. Finally one dimensional spectra are extracted for all science targets using the optimal scheme of Horne (1986) and are rebinned into logarithmic wavelength bins with 15 km s^{-1} per pixel. Sample one-dimensional spectra are shown in Figure 4.

Spectra from the multi-tier mask NGC 205-4 were reduced using a combination of IRAF multi- and long-slit tasks similar to the method described in Geha et al. (2002). The flat-field exposure for this mask was used to trace the ends of each slitlet. The APALL task was used in “strip” mode to extract and rectify two-dimensional rectangular strips for each slitlet; a similar extraction was applied to the arc lamp calibration and science frames. Data reduction proceeded on these rectified strips. Each strip was divided by its corresponding normalized flat-field image. Individual science exposures were cleaned of cosmic rays and combined. A wavelength solution was determined for each slitlet from the combined Kr/Ar/Ne/Xe arc lamp spectrum and was applied to the data. One-dimensional spectra were then extracted from each strip and rebinned into logarithmic wavelength bins with 20 km s^{-1} per pixel.

2.4. Radial Velocities

Radial velocities were measured for spectra extracted from the four DEIMOS masks by cross-correlating the observed spectra with a series of high signal-to-noise stellar templates originally created for the Sloan Digital Sky Survey covering a wide range of stellar spectral type (Cooper et al. 2006). These templates were rebinned to match the final wavelength resolution of the observations of 15 and 20 km s^{-1} per pixel for the conventional and multi-tier masks, respectively. The science and template spectra were continuum-subtracted; the template was then shifted and scaled to minimize the reduced- χ^2 . A heliocentric correction was applied to all the measured radial velocities. The fitted velocities were visually inspected and assigned a quality code to indicate the reliability of the measured redshift and the overall quality of the spectrum.

Radial velocities for individual stars were successfully measured for 769 of the 869 extracted spectra. Of the 100 spectra for which we did not measure a redshift, 51 spectra were unusable due

to bad columns or vignetting and 49 spectra had insufficient signal-to-noise ratios to determine a redshift. Of the spectra with measured velocities, 3 were background galaxies and 41 were duplicate measurements. Duplicate measurements are used to estimate our velocity error bars as discussed below. The final sample consists of 725 unique stellar radial velocity measurements.

We estimate the accuracy of our radial velocity measurements via repeat measurements of stars across the four observed masks. Twenty-nine duplicate stars were observed across the three conventional mask. Twelve stars on the multi-tier mask were duplicated on the conventional masks. The root-mean-square (rms) radial velocity difference between pairs of measurements for stars on the conventional masks is 16.3 km s^{-1} . Assuming the measurement uncertainty is the same for each member of the pair, the radial velocity error for an individual measurement is $\sqrt{2}$ times smaller than the rms of the difference, or 11.5 km s^{-1} . The rms difference between the conventional and multi-tier mask is 21.7 km s^{-1} ; this rms difference is larger than the conventional masks due to lower spectral resolution and the smaller available wavelength region in the multi-tier design. Assuming velocity errors between the conventional and multi-tier mask add in quadrature, the radial velocity error on individual multi-tier measurements is 18.4 km s^{-1} . Velocity measurements for individual stars are listed in Table 3.

3. Results

The measured velocities of individual stars allow us to probe the dynamics of NGC 205 to much larger radius than possible via integrated-light spectroscopy. In Figure 5, we show the distribution of radial velocities of individual RGB stars in the four Keck/DEIMOS slitmasks. The distribution of velocities in slitmasks N205-1 and N205-4 is centered on the systemic velocity of NGC 205. The systemic velocity of NGC 205 is $v_{\text{sys}} = -246 \pm 1 \text{ km s}^{-1}$ based on the median velocity of stars with semi-major axis distances less than $5'$. The two slitmasks off-center from NGC 205 show skewed velocity distributions. The mask N205-2, placed to the NW of NGC 205 on the farside from M31, is skewed toward more positive velocities than the NGC 205 systemic velocity; mask N205-3, to the SE of NGC 205 nearer to M31, has more negative velocities relative to the NGC 205 systemic. To illustrate this observation, we fit a Gaussian profile to the combined distribution of velocities (Figure 5, bottom panel). The fitted Gaussian has a central velocity of -246 km s^{-1} in agreement with the systemic velocity of NGC 205 measured above, and a velocity width of 42 km s^{-1} in agreement with the average velocity dispersion of NGC 205 measured by Simien & Prugniel (2002). In the four top panels of Figure 5 we plot the scaled Gaussian profile; the excess of stars in mask N205-2 and N205-3 is clearly visible to the right and left, respectively of the main velocity peak. In all four masks, there are a small number of stars with velocities less negative than NGC 205 due to foreground contamination, while the tail of stars to more negative velocities are primarily M31 halo stars whose systemic velocity is -300 km s^{-1} . We estimate M31 contamination fractions in our sample in § 3.2.

A semi-major axis distance is assigned to each slitlet based on its minimum distance to the

major axis of NGC 205. The major-axis of NGC 205 is shown in Figure 3 and was determined from surface brightness ellipse fitting by Choi et al. (2002) based on wide-field *B*-band images of NGC 205, corrected for the underlying light of M31. The major-axis of NGC 205 forms a gentle 'S' curve as plotted in Figure 3. For each slitlet, we determine its minimum distance to the major-axis and assign the semi-major axis length (a) at the point. Although there are alternative methods to assign this distance (e.g. the semi-major distance corresponding to the nearest elliptical isophote), this method most closely resembles integrated-light spectroscopy of more distant dEs to which we will compare our results.

3.1. The Velocity Profile of NGC 205

In Figure 6, we present the major-axis velocity profile for NGC 205 determined from the combined velocity measurements of RGB stars. Individual stellar velocity measurements are shown in the top panel of this figure. To determine the ensemble major-axis velocity profile, individual measurements were binned into minimum $1'$ radial bins with 25 or more stars per bin. The velocity in each bin was determined by simultaneously fitting a double Gaussian profile to the distribution of stars in that bin. To account for contamination from M31 stars, one of the two fitted Gaussian profiles had a fixed mean and velocity width of -300 km s^{-1} and 150 km s^{-1} , respectively, corresponding to best estimates for M31's halo (see § 3.2). We fit for the width and mean of the second Gaussian profile to determine both the velocity and velocity dispersion of NGC 205 in each radial bin. The relative height of these two profiles is fixed based on the M31 contamination fraction determined by maximum likelihood fitting in § 3.2. We have also run fits in which the contamination fraction is a free parameter which does not change the resulting profile appreciably. The resulting velocity and velocity dispersion profile as a function of radius is shown in the bottom two panels of Figure 6. The velocity dispersion profile is determined using a coarser binning scheme of 50 or more stars per radial bins. Error bars were computed based on number statistics in each radial bin which dominate over the radial velocity measurement errors of individual stars. We list the velocity and velocity dispersion as a function of semi-major axis distance, right ascension and declination in Table 4.

We determine the maximum major-axis rotation velocity, v_{\max} , for NGC 205 by differencing the maximum/minimum velocity in the upper-left quadrant and lower-right quadrant of Figure 6, and dividing this number by two. The maximum rotation velocity for NGC 205 is $v_{\max} = 11 \pm 5 \text{ km s}^{-1}$. The peak rotation velocity occurs at slightly different radii on either side of the galaxy, with an average radius of $r_{\max} = 4.5'$ (1.1 kpc). Our value is somewhat smaller, but within the 1-sigma error bars, of the value measured by Simien & Prugniel (2002) of $13 \pm 2 \text{ km s}^{-1}$ at $r = 4'$ based on integrated-light measurements. The Simien & Prugniel data hint at a flattening in the velocity profile, but the integrated-light data is noisy at these large radii. We observe this turnover conclusively and note that v_{\max} is the physical, rather than a observational, maximum rotation velocity. Previous observations of dE galaxies have not reached sufficient radii to observe a definite

turnover in the rotation curve; this is the first dE galaxy in which the *maximum* rotation velocity has been measured.

We plot the ratio of the maximum rotational velocity to the average velocity dispersion (v_{\max}/σ) versus ellipticity in Figure 7. We assume an ellipticity for NGC 205 of $\epsilon = 0.43$ (Choi et al. 2002), and a velocity dispersion of $\sigma = 35 \pm 5 \text{ km s}^{-1}$ determined from our profile excluding data beyond the tidal radius. The observed ratio for NGC 205 is $v_{\max}/\sigma = 0.21$. At the ellipticity of NGC 205, the expected ratio for an oblate, isotropic, rotationally-flattened body seen edge-on is slightly more than unity (Binney & Tremaine 1987). NGC 205 lies midway between a rotationally supported and anisotropic object. Interestingly, it was early kinematic observations of NGC 205 which established the paradigm that dE galaxies are supported by anisotropic velocity dispersions in contrast to rotationally supported normal ellipticals (Bender & Nieto 1990). In Figure 7, we compare NGC 205 to a sample of similar luminosity dEs in the Virgo Cluster taken from Geha et al. (2003). The Virgo dEs naturally fall into “rotating” and “non-rotating” categories. NGC 205 does not fall into either category having a mixture of both rotational and anisotropic support.

At a radius of $r \sim 4.5'$, the velocity profile of NGC 205 turns over; stars beyond this radius rotate in a direction opposite that of the main galaxy body. This turnover is in the sense that stars on the side of NGC 205 closest to M31 move with more negative velocities (approaching the systemic velocity of M31) and stars on the farside move with less negative velocities. The turnover radius is coincident with the onset of isophotal twisting as observed by Choi et al. (2002), suggesting that the outer dynamics of NGC 205 have been affected by the processes of tidal stripping. We discuss further evidence for tidal interactions and its significance in § 4.

3.2. Contamination from M31 Stars and Maximum-Likelihood Analysis

NGC 205 lies merely $40'$ (8 kpc) in projection from the center of M31 and our kinematic sample is likely contaminated with stars associated with M31. We consider two sources for contamination, the M31 disk and halo. We estimate that contamination from M31’s disk is negligible: NGC 205 lies behind M31 and its line-of-sight intersects the M31 disk at a point 37 kpc (7 scale lengths) along the disk from the center of M31 (assuming an inclination angle of the M31 disk of 12.5° and a disk scale length of 5.3 kpc (Walterbos & Kennicutt 1988)). At this scale length, the M31 disk surface brightness is $\mu_B = 29.2 \text{ mag arcsec}^{-2}$. In comparison, at the average radial distance of our spectroscopic sample ($r = 5'$), the surface brightness of NGC 205 is $\mu_B = 25.4 \text{ mag arcsec}^{-2}$. Thus, our kinematic sample is unlikely to contain stars from the disk of M31.

We estimate the contamination fraction from stars in the M31 halo based on maximum likelihood fitting. We assume the M31 halo is spherically symmetric with a power-law surface brightness profile. We normalize the surface brightness (SB) of the halo at the center of NGC 205, defining the free parameter f_0 to be the fractional contamination at the center of NGC 205. The M31 halo

surface brightness at the position of a given slitlet i is then:

$$\text{SB}_i^{\text{M31}} = f_0 \text{ SB}_0^{\text{N205}} \left(\frac{r_i^{\text{M31}}}{r^{\text{M31-N205}}} \right)^\alpha \quad (1)$$

where the angular distance between M31 and NGC 205 is $r^{\text{M31-N205}} = 40'$, the angular distance from slitlet i to the center of M31 is r_i^{M31} , and the free parameter α is the power-law index of the halo profile. The surface brightness profile of NGC 205 is based on a high-order fit to the photometry of Choi et al. (2002) with a central B -band surface brightness of $\text{SB}_0^{\text{N205}} = 19.2$ mag arcsec $^{-2}$. We assume a Gaussian velocity distribution for the M31 halo with a velocity dispersion of width σ^{M31} and a systemic velocity of $v_{\text{sys}}^{\text{M31}} = -300$ km s $^{-1}$ (Guhathakurta et al. 2004). Given a measured velocity of v_i for slitlet i , the probability that it was drawn from the velocity distribution of the M31 halo is:

$$P_i^{\text{M31}} = \frac{1}{\sqrt{2\pi}\sigma^{\text{M31}}} \exp \left[-\frac{1}{2} \left(\frac{v_i - v_{\text{sys}}^{\text{M31}}}{\sigma^{\text{M31}}} \right)^2 \right] \quad (2)$$

Similarly, the probability that a given velocity is drawn from velocity distribution of NGC 205, P_i^{N205} , is the same as Eqn. (2), however σ^{N205} and $v_{\text{sys}}^{\text{N205}}$ are the measured quantities as a function of radius. The final probability function for each slitlet i is:

$$P_i = C_i [\text{SB}_i^{\text{N205}} P_i^{\text{N205}} + \text{SB}_i^{\text{M31}} P_i^{\text{M31}}] \quad (3)$$

The normalization constant $C_i \equiv 1/(\text{SB}_i^{\text{N205}} + \text{SB}_i^{\text{M31}})$ is defined such that the integral over P_i is equal to unity. The probability P_i is evaluated for each slitlet and the natural logarithm of this quantity is summed over all slits. We do a gridded parameter search over the free parameters f_0 , σ^{M31} , and α and maximize the function $M = \sum_i \ln(P_i)$. As shown in the left panel of Figure 8, the best fitting parameters which maximize the quantity M are: $f_0 = 0.065$, $\sigma_{\text{M31}} = 150$ km s $^{-1}$ and $\alpha = -2.25$. We note that these best fitting M31 halo parameters are in good agreement with the measured M31 halo velocity dispersion by Guhathakurta et al. (2004) and an r^{-2} halo surface brightness profile.

In the right panel of Figure 8, we plot the fractional contamination in our kinematic sample from the M31 halo as a function of distance from the center of NGC 205 using the best fit parameters determined above. At the center of NGC 205, the best estimate of the contamination from M31 is 6%; this corresponds to 1.5 out of 25 stars per radial bin. On the side of NGC 205 closest to M31 the contamination is 20%, while on the farside the contamination is less than 3%. The average halo contamination fraction for our sample is 6.5%.

4. The Tidal Disruption of NGC 205

The outer dynamics of NGC 205 place significant constraint on the tidal interaction between NGC 205 and its parent galaxy M31. While the main body of NGC 205 is rotating with a maximum velocity of 11 km s $^{-1}$, the major-axis velocity profile turns over abruptly at a radius of 4.5' (1 kpc);

stars at larger radii are moving in the opposite direction than the main galaxy body. The turnover radius coincides with the onset of isophotal twisting (Hodge 1973; Kent 1987) and a downward break in the surface brightness profile (Choi et al. 2002). Both features have been demonstrated by Choi et al. to be hallmarks of tidal stripping. We make a simple estimate of the tidal radius of NGC 205, assuming NGC 205 and M31 to be point masses. We adopt a physical separation distance between these two galaxies of $r_{N205-M31} = 40$ kpc, the mass of M31 inside this distance of $M_{M31} = 1 \times 10^{11} M_{\odot}$ (Geehan et al. 2005) and the total mass of NGC 205 $M_{N205} = 2 \times 10^9 M_{\odot}$ (calculated from the maximum rotation velocity and velocity dispersion at the turnover radius). The tidal radius is calculated to be $r_{\text{tidal}} \sim 4'$ (1.0 kpc). The observed velocity turnover in NGC 205, at roughly this distance, is therefore due to tidal stripping from M31; stars beyond this radius are no longer bound to NGC 205.

The stellar motion beyond the tidal radius of NGC 205 suggests that it is on a prograde encounter with its parent galaxy: the spin angular momentum vector and the orbital angular momentum vector are parallel. The eventual destruction of a satellite on a prograde orbit is expected to proceed more slowly and create less spectacular tidal tails than one on a retrograde orbit (e.g., compare Figs. 1 and 2 of Toomre & Toomre 1972). We calculate the timescale for the destruction of NGC 205 based on the dynamical friction timescale. Using Eqn. (7.26) in Binney & Tremaine (1987), we assume the orbital velocity of NGC 205 is related the velocity difference between NGC 205 and M31 ($= \sqrt{3} \times 60$ km s $^{-1}$) and calculate $t_{\text{fric}} \sim 3 \times 10^9$ years. Detailed dynamical modeling is required to determine if features in the M31 halo, such as stellar substructure (McConnachie et al. 2004), or HI clouds (Thilker et al. 2004) are indeed associated with the orbit of NGC 205.

5. Summary

We present the stellar kinematics of NGC 205 out to large radii based on Keck/DEIMOS multislit spectroscopic observations of 725 individual red giant branch stars. NGC 205 is one of the closest examples of a dwarf elliptical galaxy and the prototype of this galaxy class. Early kinematic observations of NGC 205 established the paradigm that dE galaxies are supported primarily by anisotropic velocity dispersions Bender et al. (1991). Although kinematic study of dEs outside the Local Group suggest that a fraction of dEs are indeed supported by anisotropic velocity dispersion alone (Geha et al. 2003; De Rijcke et al. 2001), NGC 205 itself has significant rotation. We measure a maximum major-axis rotation speed for the body of NGC 205 of 11 ± 5 km s $^{-1}$, implying that this galaxy is supported by a mixture of both rotational and anisotropic velocities.

The velocity profile of NGC 205 turns over at a major-axis distance of $4.5'$ (1 kpc). This turnover is due to gravitational interaction between NGC 205 and its parent galaxy M31. The motion of stars beyond the tidal radius suggest that NGC 205 is on a prograde encounter with M31. Detailed dynamical modeling should clarify what, if any, substructure in the M31 halo is associated with disruption of NGC 205 and provide insight into the on-going interactions between

these two galaxies.

We thank S. Demers and P. Battinelli for kindly providing their photometric catalogs. We also thank P. Choi, G. Laughlin, D. Kelson and R. P. van der Marel for productive and enjoyable conversations. M. G. is supported by NASA through Hubble Fellowship grant HF-01159.01-A awarded by the Space Telescope Science Institute, which is operated by the Association of Universities for Research in Astronomy. P.G. acknowledges support from NSG grant AST-0307966 and NASA/STScI grant GO-10265.02. R.M.R. acknowledges funding by grant AST-0307931.

REFERENCES

Beasley, M., Strader, J., Brodie, J., Cenarro, J., & Geha, M. 2005, ApJ, submitted

Bender, R., & Nieto, J.-L. 1990, A&A, 239, 97

Bender, R., Paquet, A., & Nieto, J.-L. 1991, A&A, 246, 349

Binggeli, B., Sandage, A., & Tammann, G. A. 1988, ARA&A, 26, 509

Binney, J., & Tremaine, S. 1987, Galactic Dynamics (Princeton, NJ, Princeton University Press, 1987)

Bullock, J. S., Kravtsov, A. V., & Weinberg, D. H. 2000, ApJ, 539, 517

Cappellari, M., Bertola, F., Burstein, D., Buson, L. M., Greggio, L., & Renzini, A. 1999, ApJ, 515, L17

Carter, D., & Sadler, E. M. 1990, MNRAS, 245, 12P

Choi, P. I., Guhathakurta, P., & Johnston, K. V. 2002, AJ, 124, 310

Cooper et al. . 2006, in prep

Corradi, R. L. M., Magrini, L., Greimel, R., Irwin, M., Leisy, P., Lennon, D. J., Mampaso, A., Perinotto, M., Pollacco, D. L., Walsh, J. R., Walton, N. A., & Zijlstra, A. A. 2005, A&A, 431, 555

De Rijcke, S., Dejonghe, H., Zeilinger, W. W., & Hau, G. K. T. 2001, ApJ, 559, L21

Dekel, A., & Silk, J. 1986, ApJ, 303, 39

Demers, S., Battinelli, P., & Letarte, B. 2003, AJ, 125, 3037

Faber, S. M., et al. 2003, in Instrument Design and Performance for Optical/Infrared Ground-based Telescopes. Edited by Iye, Masanori; Moorwood, Alan F. M. Proceedings of the SPIE, Volume 4841., 1657–1669

Ferguson, A. M. N., Irwin, M. J., Ibata, R. A., Lewis, G. F., & Tanvir, N. R. 2002, AJ, 124, 1452

Font, A. S., Johnston, K. V., Bullock, J. S., & Robertson, B. 2005

Freedman, W. L., Madore, B. F., Gibson, B. K., Ferrarese, L., Kelson, D. D., Sakai, S., Mould, J. R., Kennicutt, R. C., Ford, H. C., Graham, J. A., Huchra, J. P., Hughes, S. M. G., Illingworth, G. D., Macri, L. M., & Stetson, P. B. 2001, ApJ, 553, 47

Geehan, J., Fardal, M., Babul, A., & Guhathakurta, P. 2005, Astro-ph/0501241

Geha, M., Guhathakurta, P., & van der Marel, R. P. 2002, AJ, 124, 3073

—. 2003, AJ, 126, 1794

Guhathakurta, P., Rich, M., Reitzel, D., Cooper, M., Gilbert, K., Majewski, S., Ostheimer, J., Geha, M., K., J., & Patterson, R. 2004, Astro-ph/0406145

Haas, M. 1998, A&A, 337, L1

Hodge, P. W. 1973, ApJ, 182, 671

Horne, K. 1986, PASP, 98, 609

Ibata, R., Chapman, S., Ferguson, A. M. N., Irwin, M., Lewis, G., & McConnachie, A. 2004, MNRAS, 351, 117

Ibata, R., Irwin, M., Lewis, G., Ferguson, A. M. N., & Tanvir, N. 2001, Nature, 412, 49

Ibata, R. A., Gilmore, G., & Irwin, M. J. 1995, MNRAS, 277, 781

Kent, S. M. 1987, AJ, 94, 306

Kleyna, J. T., Wilkinson, M. I., Gilmore, G., & Evans, N. W. 2003, ApJ, 588, L21

Lee, M. G. 1996, AJ, 112, 1438

Mastropietro, C., et al. 2004

Mayer, L., Governato, F., Colpi, M., Moore, B., Quinn, T., Wadsley, J., Stadel, J., & Lake, G. 2001, ApJ, 559, 754

McConnachie, A. W., Irwin, M. J., Ferguson, A. M. N., Ibata, R. A., Lewis, G. F., & Tanvir, N. 2005, MNRAS, 356, 979

McConnachie, A. W., Irwin, M. J., Lewis, G. F., Ibata, R. A., Chapman, S. C., Ferguson, A. M. N., & Tanvir, N. R. 2004, MNRAS, 351, L94

Meylan, G., Sarajedini, A., Jablonka, P., Djorgovski, S. G., Bridges, T., & Rich, R. M. 2001, AJ, 122, 830

Moore, B., Lake, G., & Katz, N. 1998, *ApJ*, 495, 139

Peletier, R. F. 1993, *A&A*, 271, 51

Peterson, R. C., & Caldwell, N. 1993, *AJ*, 105, 1411

Reitzel, D., Guhathakurta, P., & Rich, R. 2004, *AJ*, 127, 2133

Schlegel, D. J., Finkbeiner, D. P., & Davis, M. 1998, *ApJ*, 500, 525

Simien, F., & Prugniel, P. 2002, *A&A*, 384, 371

Thilker, D. A., Braun, R., Walterbos, R. A. M., Corbelli, E., Lockman, F. J., Murphy, E., & Maddalena, R. 2004, *ApJ*, 601, L39

Toomre, A., & Toomre, J. 1972, *ApJ*, 178, 623

van Zee, L., Skillman, E. D., & Haynes, M. P. 2004, *AJ*, 128, 121

Walterbos, R. A. M., & Kennicutt, R. C. 1988, *A&A*, 198, 61

Welch, G. A., Sage, L. J., & Mitchell, G. F. 1998, *ApJ*, 499, 209

Young, L. M., & Lo, K. Y. 1997, *ApJ*, 476, 127

Table 1. NGC 205 at a Glance

Name	α (J2000) (h:m:s)	δ (J2000) ($^{\circ} : ' : ''$)	Type	Dist. (kpc)	m_B	$M_{B,0}$	ϵ	$\mu_{B,\text{eff}}$ (mag arcsec^{-2})	r_{eff} [' (kpc)]	r_{tidal} [' (kpc)]
NGC 205	00:40:22	+41:41:07	dE5	824	9.9	-15.0	0.43	23.7	2.5 (0.6)	4.5 (1.1)

Note. — The right ascension, declination, and morphological type of NGC 205 are take from NASA/IPAC Extragalactic Database (NED). We adopt the distance to NGC 205 determined by McConnachie et al. (2005). The apparent magnitude, effective surface brightness, effective radius, and ellipticity are determined from B -band photometry from Choi et al. (2002). The ellipticity ϵ is the average value measured between $0.5'$ and $5'$. The absolute magnitude is calculated assuming an extinction of $A_B = 0.27$ from Schlegel et al. (1998). The tidal radius r_{tidal} is calculated based on the assumptions outlined in § 4

Table 2. Keck/DEIMOS Multi-Slitmask Observing Parameters

Mask Name	α (J2000) (h:m:s)	δ (J2000) ($^{\circ} : ' : ''$)	PA (deg)	t_{exp} (sec)	# of slits	% useful spectra
N205-1	00:40:27.4	+41:41:30.5	0	3600	184	91%
N205-2	00:39:50.5	+41:48:41.8	-45	3600	185	85%
N205-3	00:40:53.0	+41:40:53.0	-45	3600	193	84%
N205-4	00:40:27.4	+41:41:30.5	0	3600	320	88%

Note. — Right ascension, declination, position angle and total exposure time for each Keck/DEIMOS slitmask. The final two columns refer to the total number of slitlets on each mask and the percentage of those slitlets for which a redshift was measured.

Table 3. Velocity Measurements for Individual Stars in NGC 205

Name	α (J2000) (h m s)	δ (J2000) ($^{\circ}$ ' '')	I (mag)	$(R - I)$ (mag)	v (km s $^{-1}$)	v_{err} (km s $^{-1}$)	S/N	Mask
2186	00 39 15.0	+41 53 19.8	20.7	1.03	-195.9	11.5	15.7	N205-2
2196	00 39 15.9	+41 52 23.0	20.7	0.89	-309.8	11.5	11.7	N205-2
2272	00 39 23.6	+41 50 29.5	20.7	0.93	-213.8	11.5	13.6	N205-2
2441	00 39 25.3	+41 48 39.8	20.9	0.84	-240.8	11.5	9.0	N205-2
2658	00 39 20.3	+41 52 21.7	20.9	1.30	-162.9	11.5	12.6	N205-2
2681	00 39 18.5	+41 54 13.7	21.0	0.91	-261.8	11.5	10.5	N205-2
2770	00 39 15.8	+41 51 23.7	21.0	1.07	-225.8	11.5	9.8	N205-2
2805	00 39 20.9	+41 53 40.0	21.1	0.99	-291.8	11.5	10.1	N205-2
3047	00 39 25.1	+41 52 54.9	21.2	0.77	-174.9	11.5	7.7	N205-2
3234	00 39 22.5	+41 53 31.4	21.4	0.69	-96.9	11.5	7.1	N205-2
3238	00 39 23.7	+41 51 54.1	21.4	0.66	-288.8	11.5	7.3	N205-2
3239	00 39 18.3	+41 54 02.4	21.3	0.79	-171.9	11.5	8.7	N205-2
3279	00 39 19.3	+41 52 28.5	21.3	0.90	-165.9	11.5	7.9	N205-2
3804	00 39 25.5	+41 54 17.3	21.6	0.86	-318.8	11.5	7.0	N205-2
4716	00 39 30.2	+41 50 03.2	20.1	1.87	-393.7	11.5	30.8	N205-2
4773	00 39 57.6	+41 43 02.7	20.6	0.29	-219.8	11.5	18.6	N205-2
4832	00 40 02.2	+41 42 56.5	20.8	0.64	-168.9	11.5	21.9	N205-2
4914	00 39 50.4	+41 49 56.8	20.5	0.71	-201.9	11.5	18.9	N205-2
5002	00 39 36.5	+41 48 13.7	20.6	0.78	-516.6	11.5	16.3	N205-2
5096	00 40 02.9	+41 45 56.0	20.5	1.30	-165.9	11.5	17.8	N205-2
5100	00 39 58.3	+41 48 33.2	20.5	1.35	-162.9	11.5	18.0	N205-2
5109	00 39 52.1	+41 49 38.8	20.5	1.01	-267.8	11.5	18.9	N205-2
5123	00 39 57.2	+41 48 09.3	20.6	0.97	-234.8	11.5	17.9	N205-2
...

Note. — Velocity measurements for individual stars in NGC 205. Star names, positions and magnitudes are taken from Demers et al. (2003). We list the heliocentric radial velocity (v), velocity error (v_{err}), the median per pixel signal-to-noise (S/N) and the DEIMOS mask name for each star. Velocity error bars were determined from measurement overlaps for each mask as discussed in § 2.4. We also listed the median per pixel S/N value for each slitlet in the wavelength range 8000 to 9000Å and refer the reader to Gilbert et al. (2005) for a discussion of velocity errors for individual slitlets based on the S/N. Table 4 is published in its entirety in the electronic edition of the *Astronomical Journal* and is available upon request. A portion is shown here for guidance regarding its form and content.

Table 4. Major-Axis Velocity and Velocity Dispersion Profile of NGC 205

Semi-major Dist. (arcmin)	α (J2000) (h m s)	δ (J2000) ($^{\circ}$ ' '')	v_{rot} (km s $^{-1}$)	v_{err} (km s $^{-1}$)	σ (km s $^{-1}$)	σ_{err} (km s $^{-1}$)
−17.3	00 41 12.4	+41 29 19.7	−299.1	8.9		
−14.0	00 41 01.5	+41 31 25.3	−292.0	10.0	34.4	9.4
−10.8	00 40 53.5	+41 33 42.1	−267.1	9.2		
−8.4	00 40 42.3	+41 34 46.9	−258.5	4.7	35.6	7.6
−7.0	00 40 32.3	+41 34 46.2	−247.2	6.7		
−6.0	00 40 25.9	+41 35 08.5	−241.4	8.5	44.9	7.4
−5.0	00 40 23.9	+41 36 09.0	−232.6	5.3		
−4.0	00 40 22.1	+41 37 07.0	−239.6	5.5	30.0	5.0
−3.0	00 40 23.6	+41 38 11.8	−239.0	3.9		
−2.0	00 40 24.4	+41 39 12.6	−239.4	3.9	27.2	4.9
−1.0	00 40 28.4	+41 40 20.3	−243.0	5.3		
0.0	00 40 30.4	+41 41 22.9	−246.9	5.7	22.4	6.0
1.0	00 40 26.3	+41 42 15.8	−249.9	3.8		
2.0	00 40 21.0	+41 43 05.9	−253.5	3.1	35.7	4.9
3.0	00 40 18.9	+41 44 04.2	−254.1	4.5		
4.0	00 40 23.8	+41 45 07.2	−253.2	3.8	37.3	6.1
5.0	00 40 22.3	+41 46 12.0	−251.1	3.8		
6.0	00 40 24.1	+41 47 38.8	−240.9	5.7	45.8	6.7
7.0	00 40 15.1	+41 47 57.1	−229.9	5.9		
8.8	00 39 58.0	+41 47 13.2	−222.7	8.3	40.1	8.3
11.5	00 39 48.7	+41 48 43.2	−218.4	6.2		
14.1	00 39 36.2	+41 49 45.8	−225.2	8.1	38.4	8.0

Note. — The major-axis velocity and velocity dispersion profile determined from the combined measurements of individual RGB stars. Positive radial bins correspond to the NW side of NGC 205, on the side of NGC 205 farthest from M31. The profiles are determined along the major-axis of NGC 205 which forms a gentle 'S' curve as shown in Figure 3.

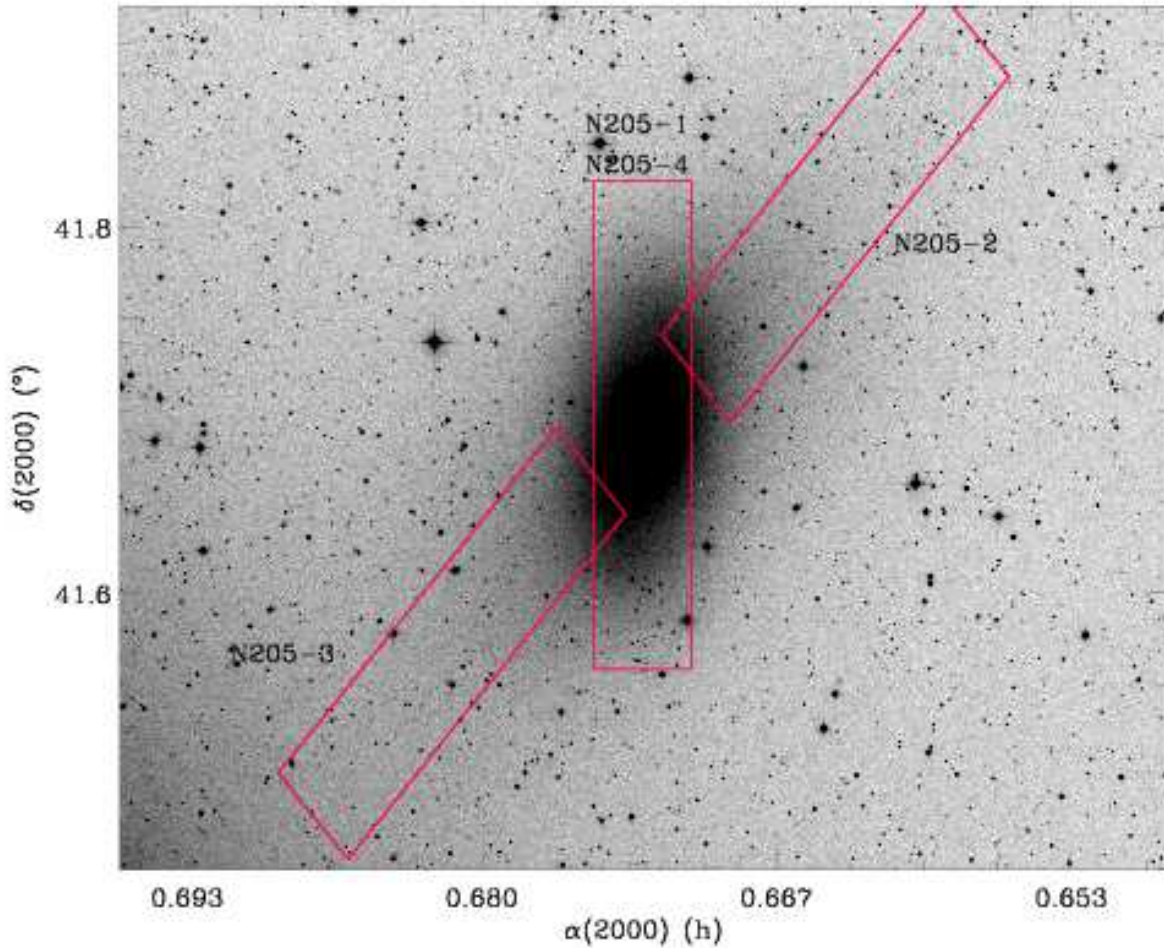


Fig. 1.— Digitized Palomar Sky Survey image of NGC 205 showing the placement of the four DEIMOS slitmasks (N205-1 through N205-4). The image is $42' \times 28'$; North is up, East is to the left. The disk of M31 can be seen in the bottom left (South-East) corner of the image.

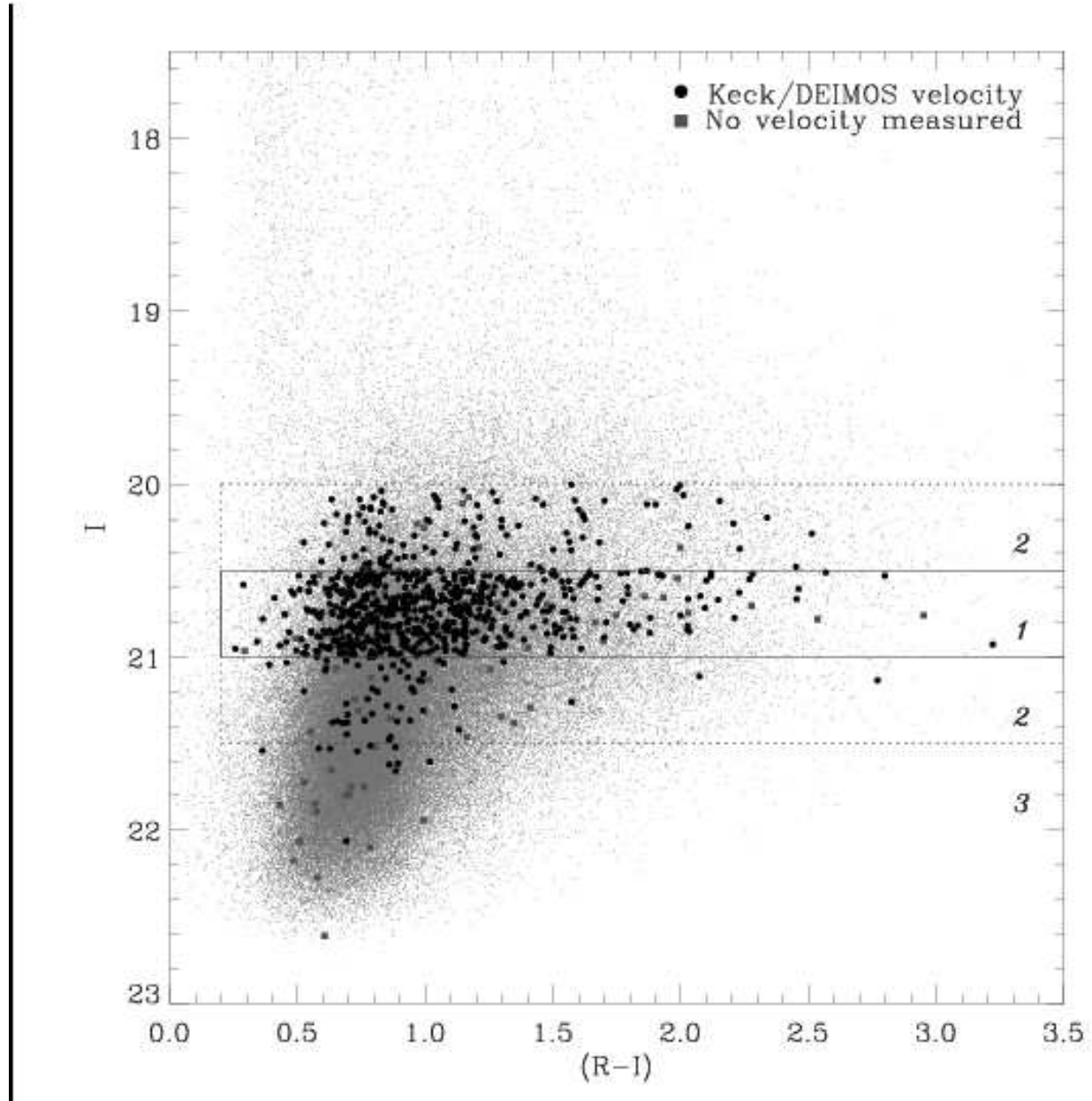


Fig. 2.— Color-magnitude diagram based on Demers et al. (2003) R - and I -band CHFT12K photometry in a $42' \times 28'$ region centered on NGC 205. Large symbols indicate objects targeted for DEIMOS spectroscopy in this study: black circles are targets with measured velocities, grey squares are targets for which no velocity could be measured. The numbered boxes indicate the location of our primary (1), secondary (2) and tertiary (3) spectroscopic priorities.

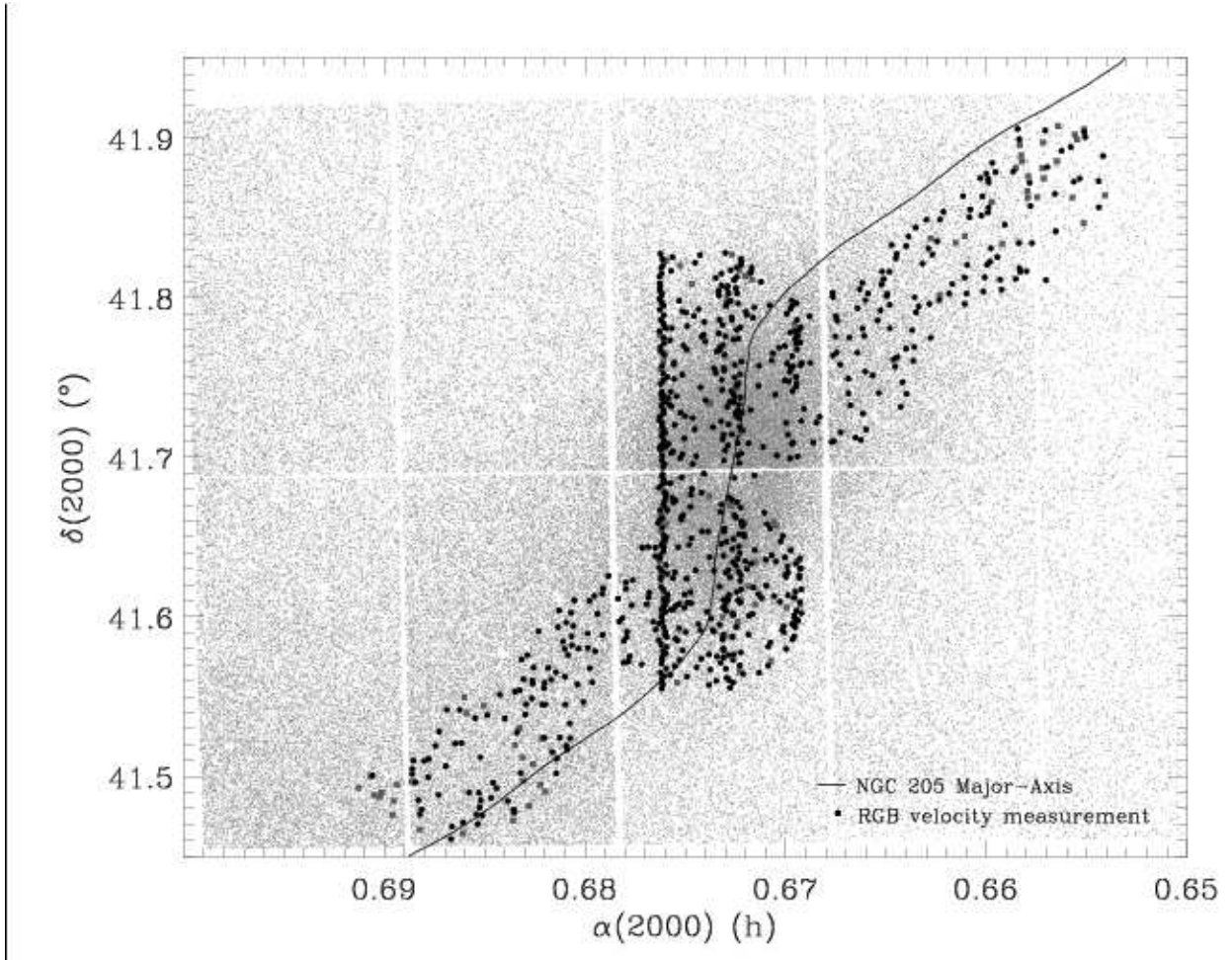


Fig. 3.— Spatial distribution of stars in NGC 205 (small grey points) from Demers et al. (2003) photometry. Large symbols indicate objects targeted for DEIMOS spectroscopy; the tiered pattern of slitlets can be seen in the central mask. The solid curve is the major axis of NGC 205 determined from Choi et al. (2002) photometry.

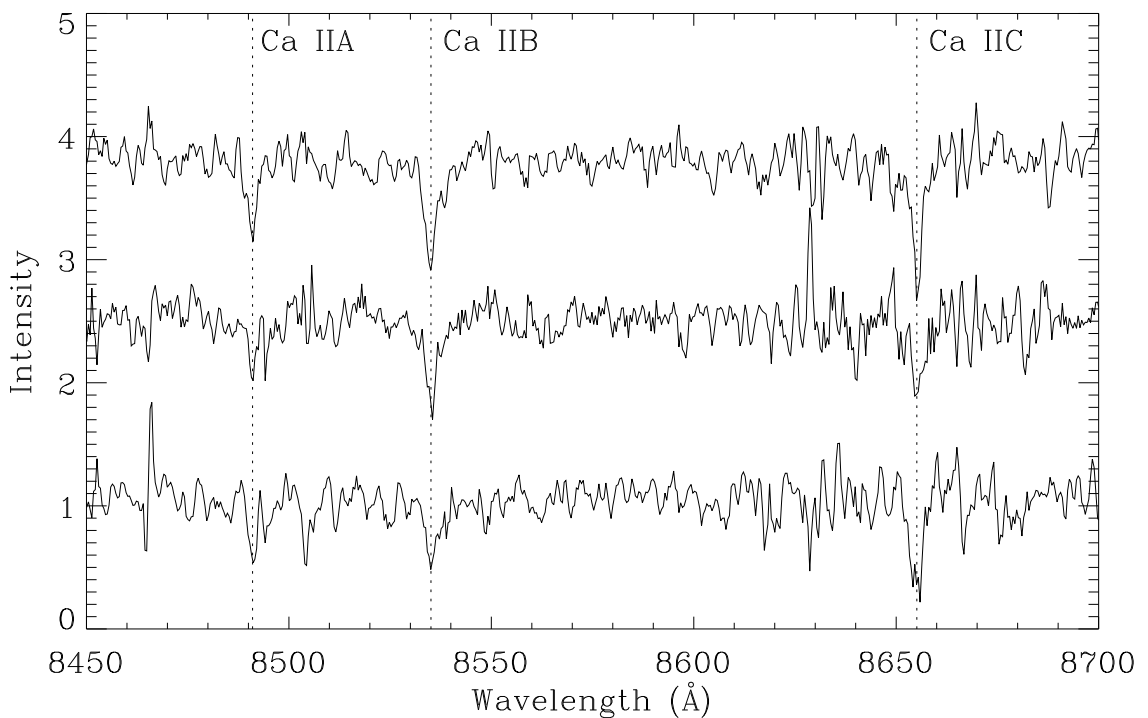


Fig. 4.— Representative one-dimensional Keck/DEIMOS spectra of RGB stars in NGC 205 centered on the Ca II region. We compare spectra from three slitlets in the inner region of NGC 205.

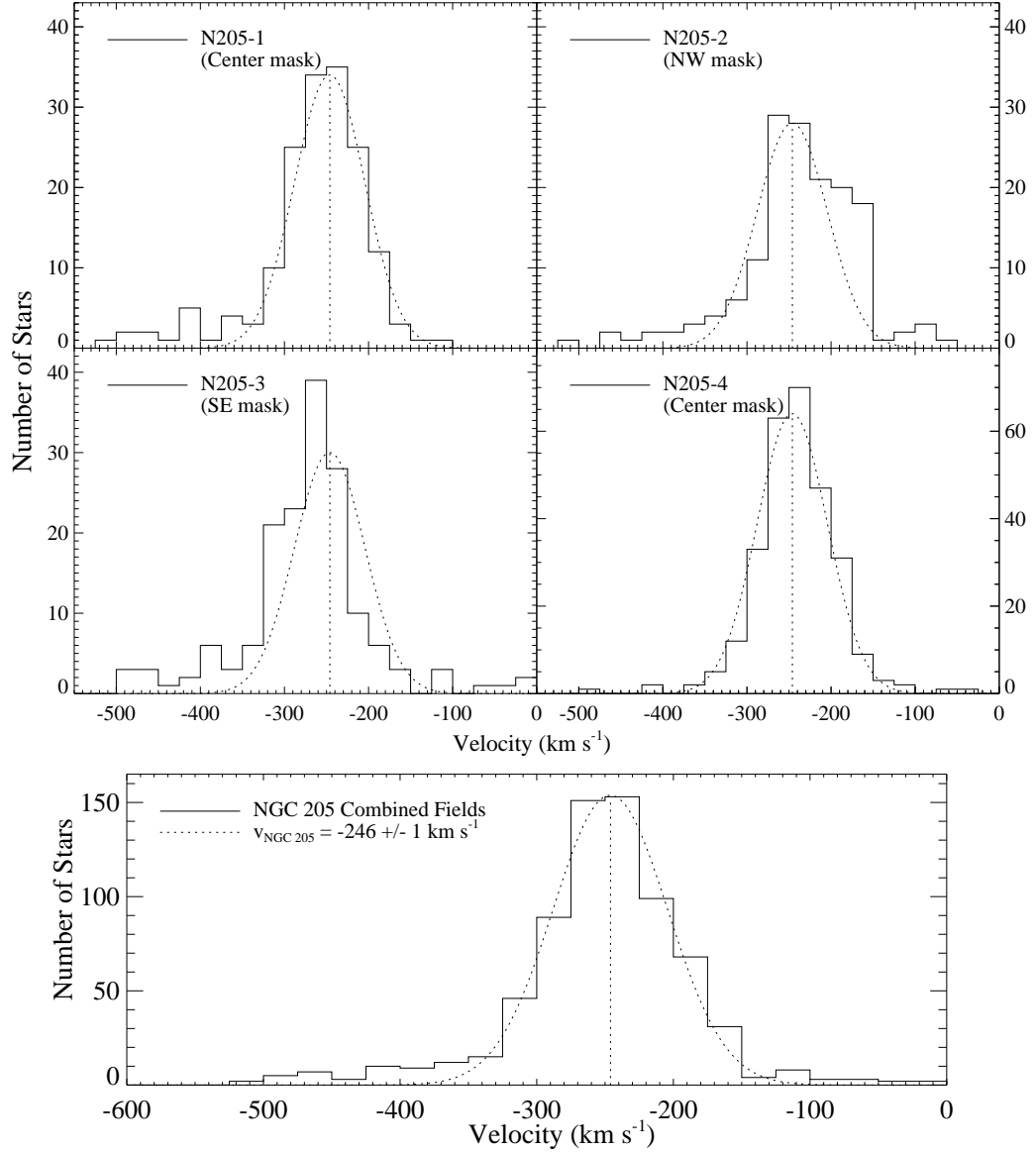


Fig. 5.— Velocity histograms for the four observed DEIMOS masks in NGC 205 (*top four panels*) and the combined fields (*bottom*). A Gaussian profile, fit to the combined velocity distribution, is plotted as the dotted curve in each panel. The Gaussian profile has a central velocity of $v_{\text{sys}} = -246 \text{ km s}^{-1}$ and a velocity width of 42 km s^{-1} . The height of the Gaussian has been scaled to the distribution of velocities in each individual panel. The masks N205-2 and N205-3, located on opposite sides of the center of NGC 205 along the major axis/tidal extension, display asymmetry in their velocity histograms towards more positive and negative velocities, respectively. This is a result of internal rotation and tidal distortion in the dE galaxy.

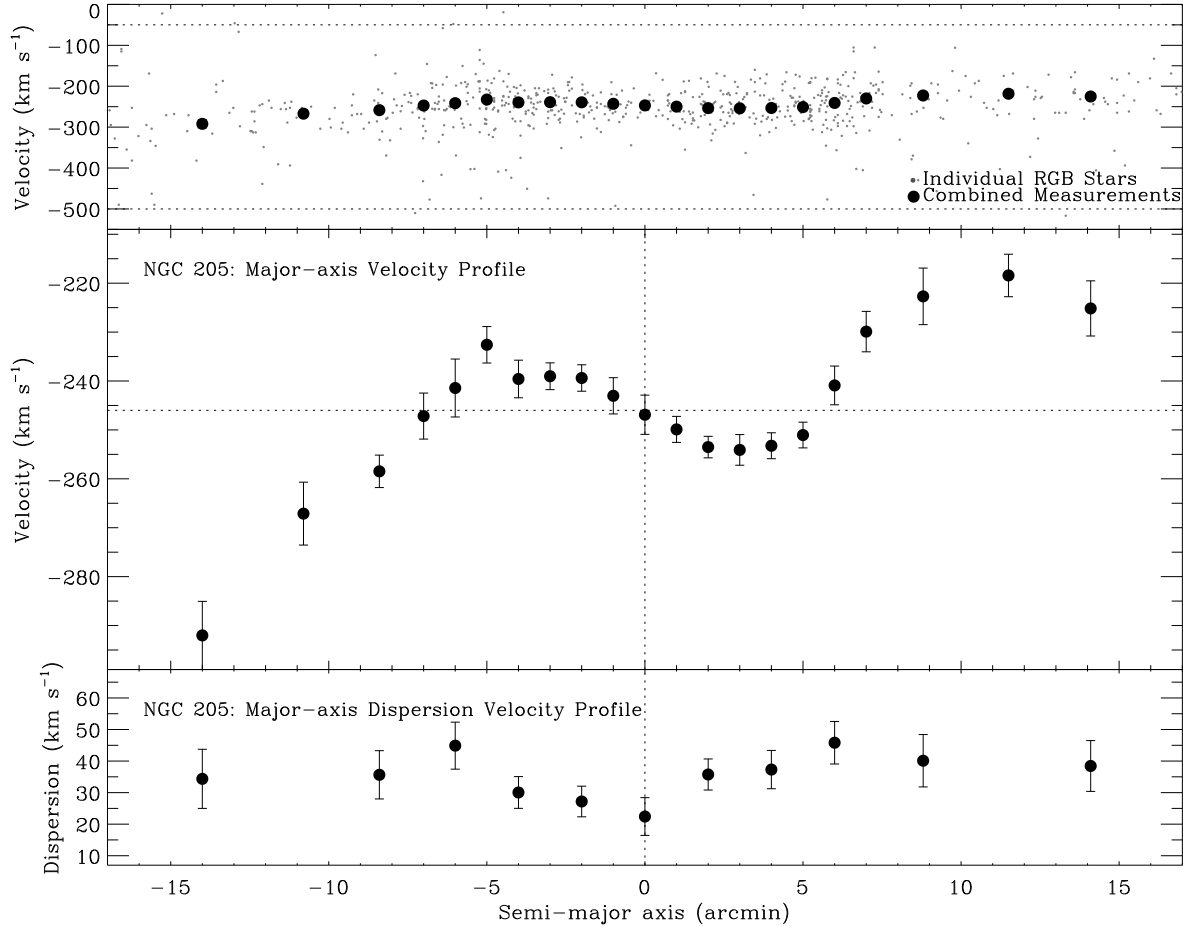


Fig. 6.— Major-axis velocity profile for NGC 205. (Top) Small grey symbols indicate Keck/DEIMOS velocity measurements of individual RGB stars, larger black symbols are the combined velocity measurements based on Gaussian fits to the velocity distribution in each radial bin. Dotted lines indicate the limits inside which the combine measurements are determined. (Middle) Combined velocity measurements (same as top panel) with a finer velocity scale. The vertical dotted line is plotted at galaxy center; the horizontal dotted line is plotted at the measured systemic velocity of NGC 205. (Bottom) Velocity dispersion profile for NGC 205 determined using a coarser binning scheme than the velocity profile.

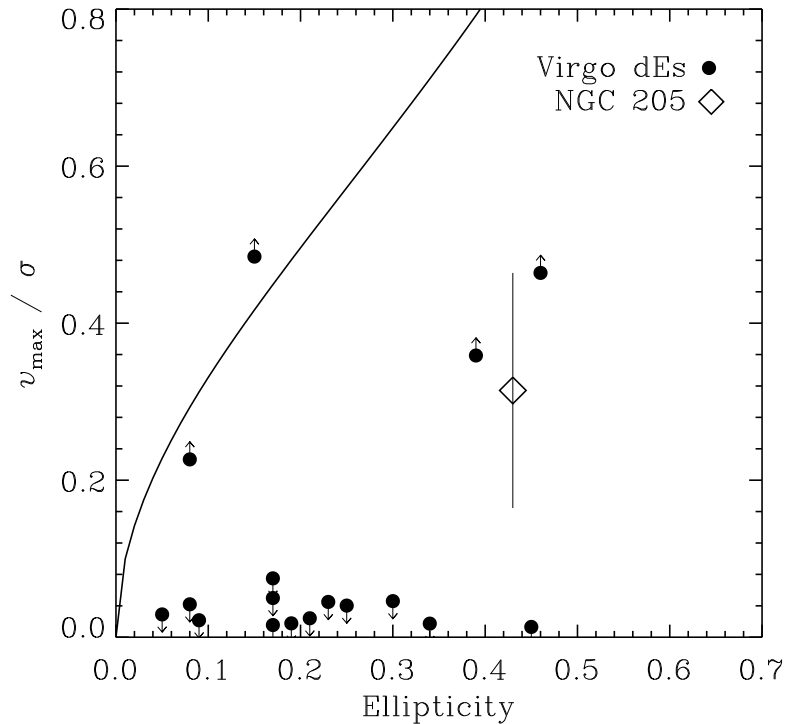


Fig. 7.— The ratio of the rotation velocity v_{\max} to velocity dispersion σ plotted versus mean isophotal ellipticity. The solid line is the expected relation for an oblate, isotropic galaxy flattened by rotation. Solid symbols indicate Virgo Cluster dEs from Geha et al. (2003), the open diamond is NGC 205. Unlike the Virgo dEs, NGC 205 has a mixture of both rotational and anisotropic support.

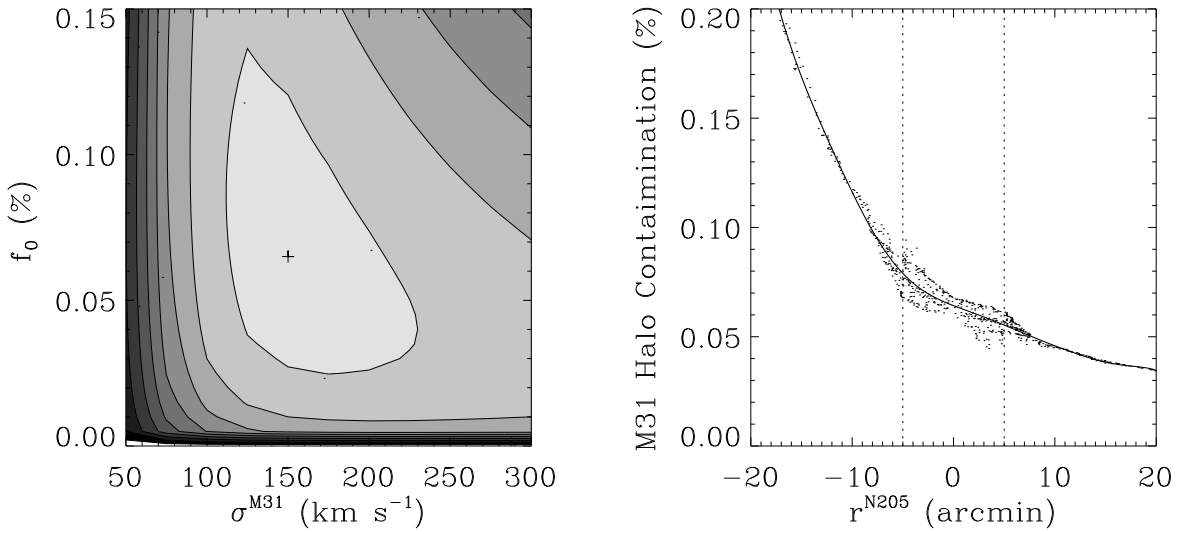


Fig. 8.— (Left) Likelihood contours of the contamination fraction of M31 stars (f_0) versus the velocity dispersion of the M31 halo. The third free parameter in our model, the power-law index of the M31 halo profile, is fixed at the best-fit value of $\alpha = -2.25$. The “+” symbol indicates the best fitting model parameters of $f_0 = 0.065$ and $\sigma_{M31} = 150 \text{ km s}^{-1}$. (Right) M31 halo contamination fraction as a function of position in NGC 205. The average contamination from M31 halo stars for the sample is 6.5%. The vertical dotted lines indicate the radius of the turnover in the major-axis velocity profile.